An Ultrasound Matrix Transducer for High-Frame-Rate 3-D Intra-cardiac Echocardiography

dos Santos, Djalma Simões; Ossenkoppele, Boudewine; Hopf, Yannick M.; Soozande, Mehdi; Noothout, Emile; Vos, Hendrik J.; Bosch, Johan G.; Pertijs, Michiel A.P.; Verweij, Martin D.; de Jong, Nico

DOI
10.1016/j.ultrasmedbio.2023.11.001

Publication date
2024

Document Version
Final published version

Published in
Ultrasound in Medicine and Biology

Citation (APA)
dos Santos, D. S., Ossenkoppele, B., Hopf, Y. M., Soozande, M., Noothout, E., Vos, H. J., Bosch, J. G., Pertijs, M. A. P., Verweij, M. D., & de Jong, N. (2024). An Ultrasound Matrix Transducer for High-Frame-Rate 3-D Intra-cardiac Echocardiography. *Ultrasound in Medicine and Biology*, *50*(2), 285-294. https://doi.org/10.1016/j.ultrasmedbio.2023.11.001

Ultrasound in Medicine & Biology 50 (2024) 285−294

Contents lists available at ScienceDirect

Ultrasound in Medicine & Biology

journal homepage: www.elsevier.com/locate/ultrasmedbio

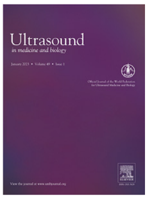

Original Contribution

An Ultrasound Matrix Transducer for High-Frame-Rate 3-D Intra-cardiac Echocardiography

Djalma Simões dos Santos [a,*], Boudewine Ossenkoppele [a], Yannick M. Hopf [b], Mehdi Soozande [c], Emile Noothout [a], Hendrik J. Vos [a,c], Johan G. Bosch [c], Michiel A.P. Pertijs [b], Martin D. Verweij [a,c], Nico de Jong [a,c]

[a] Laboratory of Medical Imaging, Department of Imaging Physics, Delft University of Technology, Delft, The Netherlands
[b] Electronic Instrumentation Laboratory, Delft University of Technology, Delft, The Netherlands
[c] Department of Biomedical Engineering, Thoraxcenter, Erasmus Medical Center, Rotterdam, The Netherlands

ARTICLE INFO

Keywords:
Ultrasound transducer
Matrix array
Application-specific integrated circuit
High frame rate
Three-dimensional
Intra-cardiac echocardiography

Objective: Described here is the development of an ultrasound matrix transducer prototype for high-frame-rate 3-D intra-cardiac echocardiography.
Methods: The matrix array consists of 16 × 18 lead zirconate titanate elements with a pitch of 160 µm × 160 µm built on top of an application-specific integrated circuit that generates transmission signals and digitizes the received signals. To reduce the number of cables in the catheter to a feasible number, we implement subarray beamforming and digitization in receive and use a combination of time-division multiplexing and pulse amplitude modulation data transmission, achieving an 18-fold reduction. The proposed imaging scheme employs seven fan-shaped diverging transmit beams operating at a pulse repetition frequency of 7.7 kHz to obtain a high frame rate. The performance of the prototype is characterized, and its functionality is fully verified.
Results: The transducer exhibits a transmit efficiency of 28 Pa/V at 5 cm per element and a bandwidth of 60% in transmission. In receive, a dynamic range of 80 dB is measured with a minimum detectable pressure of 10 Pa per element. The element yield of the prototype is 98%, indicating the efficacy of the manufacturing process. The transducer is capable of imaging at a frame rate of up to 1000 volumes/s and is intended to cover a volume of 70° × 70° × 10 cm.
Conclusion: These advanced imaging capabilities have the potential to support complex interventional procedures and enable full-volumetric flow, tissue, and electromechanical wave tracking in the heart.

Introduction

Arrhythmia is an abnormal rhythm of the heart that results from disruptions or irregularities in the electrical signals that regulate the heart's beating. These disruptions can cause the heart to beat too fast, too slow, or in an irregular pattern, which can affect the heart's ability to pump blood effectively. The most frequently occurring arrhythmia is atrial fibrillation, which is the major cardiac cause of stroke [1]. According to estimates, more than 5.6 million people will experience this condition in the United States by 2050 [2], while in the European Union, the number is expected to reach 17.9 million by 2060 [3]. Atrial fibrillation can initially be treated with drugs, but in some cases, catheter ablation may be necessary [4]. Ablation is a procedure that uses heat, cold, or radiofrequency waves to create small scars on the heart tissue, disrupting the abnormal electrical signals responsible for an irregular heartbeat and restoring the normal rhythm and activation patterns of the heart [5].

Since the inception of ablation procedures, X-ray fluoroscopy has been employed to provide guidance because of its large field of view and ability to clearly visualize catheters and other devices. However, fluoroscopy also has significant disadvantages. First, ionizing radiation exposure has potentially harmful effects on the practitioner and the patient and hence imaging time is severely limited. Second, fluoroscopy provides limited visualization of atrial tissues, which can make it difficult to identify and target specific areas of interest. To overcome this limitation, the practitioner must rely on the combination of visual landmarks and subtle catheter sensations [6]. However, this approach can increase the risk of incomplete ablation or damage to surrounding tissues, leading to complications or the need for additional procedures [7].

As an alternative to relying solely on fluoroscopy, intra-cardiac ultrasound imaging can be used in combination with fluoroscopy to provide complementary imaging guidance, leading to improved accuracy and safety during interventional procedures [6]. In intra-cardiac

---

* Corresponding author. Delft University of Technology, Lorentzweg 1, Building 22, Room D206, 2628 CJ Delft, The Netherlands.
E-mail address: D.SimoesdosSantos@tudelft.nl (D.S. dos Santos).
Djalma Simões dos Santos and Boudewine Ossenkoppele contributed equally to this work.

https://doi.org/10.1016/j.ultrasmedbio.2023.11.001
Received 28 June 2023; Revised 31 October 2023; Accepted 1 November 2023

echocardiography (ICE), a catheter containing a miniature ultrasound transducer is inserted into the cardiac cavities during the ablation procedure. This enables the practitioner to navigate the ablation catheter and visualize cardiac structures from an intra-cardiac perspective [8−10]. Integrating ICE into ablation procedures for atrial fibrillation reduces both fluoroscopy time and the occurrence of major complications significantly [7,11]. In addition to serving as a visualization tool of the cardiac structure, ultrasound can be used for electromechanical wave imaging (EWI), which is a novel ultrasound-based modality for mapping the electromechanical wave (EW), that is, the transient tissue deformations occurring in immediate response to the electrical activation [12−14]. Several studies have reported a high correlation between cardiac electrical activity and the consequent EW for healthy and arrhythmic cases in both simulation [15] and *in vivo* data [12−14,16,17]. Therefore, by use of EW mapping, the origin of the arrhythmia can be detected, and subsequently, ablation can be carried out on the source to terminate the arrhythmia effectively [17].

At present, EWI is performed primarily using a transthoracic transducer, which is placed on the surface of the chest. One limitation of that approach is that it is more prone to generate reflections on high-impedance materials, such as the rib cage and the pacemaker leads, leading to a poor acoustic window [14,17]. In addition, the transthoracic transducer is limited in its ability to provide high-quality imaging of certain regions of the heart that are difficult to access from the surface of the chest. To overcome these limitations and obtain a more comprehensive and accurate EW mapping, ICE imaging might be essential. An ICE device can provide both imaging guidance during interventional procedures and a map of the cardiac electromechanical activation. Furthermore, because of its proximity to the heart, ICE imaging enables the use of higher central frequencies, resulting in better axial resolution compared with transthoracic imaging [8].

As EWs move with velocities ranging from 0.5 to 2 m/s, a high frame rate is necessary to capture their rapid movement [8]. Additionally, volumetric imaging is necessary for fully visualizing the complex patterns of EW propagation. This is because the waves propagate throughout the entire heart in three dimensions, and their precise patterns of activation and conduction can be difficult to interpret from 2-D images alone [17]. Furthermore, as the activation patterns in atrial fibrillation are irregular in time and space [18,19], the EW propagation needs to be visualized within a heartbeat rather than through the combination of acquisitions across subsequent heartbeats [17,20]. Therefore, an ICE device that offers high-frame-rate 3-D imaging capability is critical for effective visualization of EW propagation [8].

Intra-cardiac echocardiography technology currently faces challenges in meeting the demands of high-frame-rate 3-D imaging. Designing ICE catheters that can handle these requirements is difficult because it requires using a 2-D matrix array with a sufficiently large aperture and a large number of elements. However, the diameter of the catheter limits the size of the aperture and the number of cables that can fit inside the shaft. To address the latter limitation, application-specific integrated circuits (ASICs) can be used in ICE probes, and the cable reduction can be achieved in various ways, including subarray beamforming, in-probe digitization, and time-division multiplexing [21−23]. In addition to reducing the number of channels, an ASIC can also amplify received signals to prevent attenuation caused by cable loading between the acoustic elements and the imaging system [24,25]. However, recent 3-D ICE designs are limited in functionality by the integration challenge. This expresses itself in the lack of integration of a transmit beamformer [26], inadequate signal-to-noise ratio (SNR) resulting from low-voltage transmit [27], receive-only architectures [6,22,28], or lower frame rates [6]. Examples of commercially available ICE catheters include the Verisight Pro from Philips [29], the ACUSON AcuNav from Siemens [30], and the NUVISION from Biosense Webster [31], which operates using GE Healthcare Vivid ultrasound systems. Although these probes offer 2-D and 3-D live imaging guidance, their frame rates are relatively low for EWI.

We have recently conducted a simulation study in which we proposed a novel imaging scheme for high-frame-rate 3-D ICE imaging using a side-looking matrix composed of 64 × 18 square elements [8]. The element pitch was 160 µm, and the center frequency was in the range 5−6 MHz. For channel count reduction, we implemented 1-D micro-beamforming in the elevation direction. Additionally, to achieve a high frame rate while covering a volume of 70° × 70° × 10 cm, we employed a technique of transmitting fan-shaped diverging beams steered across seven elevation angles, with a 20° divergence in elevation and 70° in azimuth. In simulations, the proposed method outperformed the current state of the art on 3-D ICE in terms of frame rate. The currently reported prototype transducer fits such an imaging scheme.

Here we describe the development of a side-looking ICE prototype transducer that uses an array of piezoelectric elements with a pitch of 160 µm × 160 µm integrated with a pitch-matched ASIC. Details on the circuit implementation of the building blocks of this ASIC have been reported in Hopf et al. [26]. The primary objective of this work is to determine the feasibility of this prototype for high-frame-rate 3-D ICE imaging. We provide a comprehensive analysis of the design, technical details, characterization and performance of the prototype. To our knowledge, this is the first study to report an ICE probe that is capable of generating high-frame-rate 3-D images with a wide field of view and having a digital output.

Methods

Design choices

The process of designing ICE transducers is very challenging and complex, as the size of the catheter poses significant physical limitations on both the transducer aperture and channel count. The prototype transducer herein presented is designed to fit within a 10-French catheter, which has an outer diameter of 3.3 mm. This limits the transducer aperture to approximately 3 mm in the elevation direction, while the number of cables that can be accommodated within the catheter shaft is limited to ~100 [6,9]. In our simulations [8], we have opted to use a rectangular aperture of about 10 mm × 3 mm (azimuth × elevation). The matrix array consisted of square elements with a pitch of 160 µm in both directions, resulting in a total of 64 × 18 elements. To achieve a penetration depth of up to 10 cm, we selected a center frequency of 6 MHz. Figure 1a shows a schematic representation of the proposed side-looking ICE transducer.

To achieve optimal 3-D imaging, precise control of transmit and receive time delays, as well as apodization for every element, is crucial. This requires addressing each element of the array individually [32]. As maintenance of an element pitch that is below or close to half the wavelength is desirable to avoid grating lobes [33], the resulting matrix array consists of more than a thousand elements, exceeding by far the cable limit imposed by the catheter shaft. Therefore, it is necessary to reduce the number of channels of the probe significantly.

Several techniques have been proposed to reduce the complexity of fully populated matrix arrays, including sparse matrix arrays [34,35] and row-column addressed matrix arrays [36,37]. However, these techniques have inherent limitations. Sparse matrix arrays suffer from lower SNR and higher clutter levels [38], while row−column addressed matrix arrays have more complex read-out sequences and reduced flexibility in transmit beamforming, severely complicating the implementation of a diverging wave transmission scheme as is required to insonify the full imaging volume with a small number of transmissions for high-frame-rate imaging [39]. One of the most effective ways to achieve channel reduction is by using the “micro-beamforming” technique, also known as “subarray/subaperture beamforming,” or “pre-steering” [21]. This technique performs the first step of beamforming at the probe tip using an ASIC, by dividing the array into subarrays and combining the RF signals within each subarray by means of a delay-and-sum operation. This partial beamforming reduces the number of signals that need to be

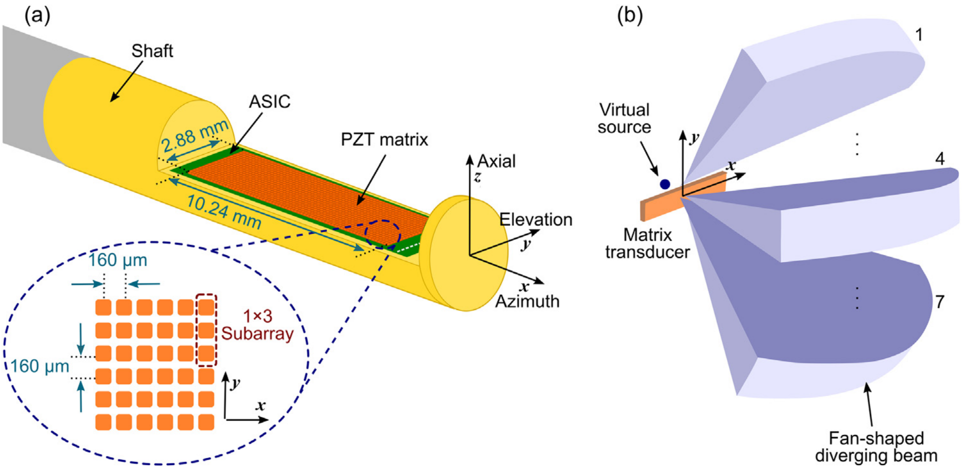

Figure 1. (a) Schematic representation of the proposed intra-cardiac echocardiography transducer. (b) Transmit scheme using fan-shaped beams.

transmitted through the cables and processed in the ultrasound system. The remaining beamforming and image reconstruction are performed in the ultrasound system [22,32]. In our design, we have opted to use micro-beamforming for channel reduction. Our approach involves dividing the array into small subarrays consisting of 1 × 3 elements, as this size offered a good balance between channel reduction and image quality according to earlier simulations [8]. With this, the number of cables was reduced by a factor of 3. Yet, a further on-chip reduction is still required to reduce the cable count sufficiently.

Imaging scheme

In our earlier work [8], we introduced a novel imaging scheme that enables volumetric imaging with a sufficiently high frame rate and image quality for EWI, while also reducing the data rate to a practical level. Our objective was to achieve a frame rate of 1000 volumes/s, with a penetration depth of up to 10 cm and an opening angle of 70° × 70°. For a depth of 10 cm, the round-trip travel time of ultrasound waves requires approximately 130 μs, assuming the speed of sound of 1540 m/s. As a result, the pulse repetition frequency (PRF) is limited to 7.7 kHz to allow enough time for the echoes to return before sending out another pulse. For this PRF and depth, a maximum of seven ultrasound pulses can be transmitted per frame to cover the entire region of interest, leading to a frame rate of 1000 volumes/s. Because we are limited to only seven transmissions to cover the entire volume, a diverging wave transmission scheme is necessary.

The proposed transmit scheme involves the use of seven fan-shaped diverging beams. These beams are steered in different directions in elevation, as illustrated in Figure 1b, and employ a 20° divergence in elevation and 70° in azimuth. We use a single virtual source to generate the desired fan-shaped diverging beam. In receive, the subarray beamformers are capable of covering a pre-steering range of ±30° in the elevation direction. To reduce grating lobes and improve image quality, we use angular weighted coherent compounding. This technique accounts for transmit beam contours such that the noise and grating lobes from non-insonified regions are suppressed, while overlapping areas from neighboring transmissions are weighted and coherently compounded, resulting in a more accurate image [40].

ASIC implementation

In Figure 2, the architecture overview of the designed ASIC is illustrated. It includes high-voltage transmitters, analog frontends, hybrid beamforming analog-to-digital converters (ADCs), and data transmission to the imaging system [26]. The element-level circuitry is 160 μm × 160 μm in size and is pitch-matched with the matrix array.

The transmit (TX) part incorporates an on-chip unipolar pulser [41] that can generate pulses up to 30 V. In addition to diverging waves, the implemented TX beamformer can produce other commonly used delay patterns, such as angled plane waves or focused waves.

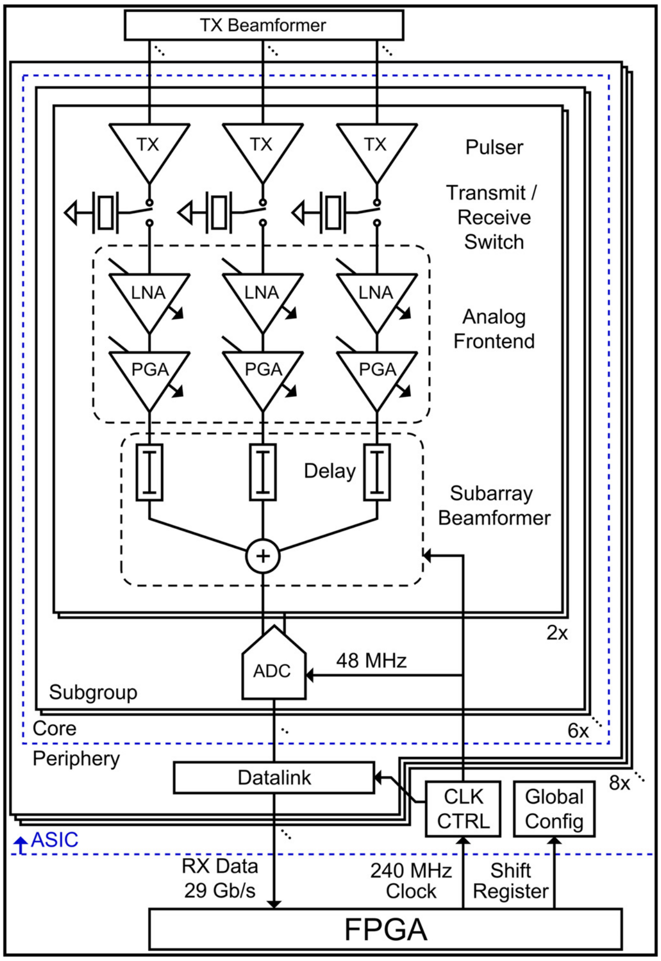

Figure 2. Block diagram of the application-specific integrated circuit architecture.

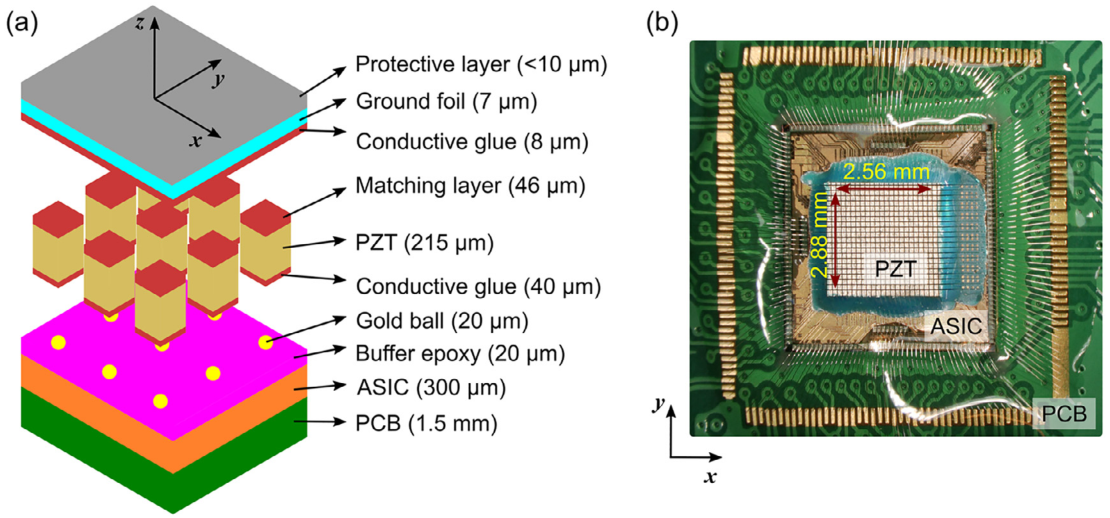

Figure 3. (a) Acoustic stack with the indication of the thickness of each layer (not drawn to scale). (b) Microscopic photo of the manufactured prototype.

In receive (RX), the signal from each element is connected to a low-noise amplifier (LNA), followed by a second-stage programmable gain amplifier (PGA) [26]. The LNA can be switched in discrete steps of 18 dB ranging from −12 to 24 dB, while the second stage can be configured in 6 dB steps ranging from 6 to 24 dB. Together, this enables the implementation of time−gain compensation (TGC) with a range of 54 dB. This is achieved through the use of 10 discrete steps of 6 dB, spanning from −6 dB to 48 dB. The outputs of three individual element-level circuits are merged using a 1 × 3-element subarray beamformer. Two of these subarrays are then combined to form a 2 × 3-element subgroup. Following this, the merged signals are digitized by an ADC at the rate of 24 MS/s with a resolution of 10 bits. The outputs are received by a periphery-level block, which provides a datalink to process the received data. To further reduce cable count in receive, a channel that combines time-division multiplexing (TDM) and four-level pulse amplitude modulation (PAM) data transmission has been implemented [42,43]. This approach, together with the subarray beamforming, results in an 18-fold reduction in cable count.

Transducer fabrication

To simplify the fabrication process of the prototype transducer, we made two key decisions. First, we chose to mount the probe onto a custom daughterboard printed circuit board (PCB) rather than assembling it into a catheter at this stage. Second, instead of building the full size of the proposed ICE transducer (a 64 × 18 matrix array), we opted to build one-quarter of the aperture in the azimuth direction, resulting in a 16 × 18 matrix array. Building a smaller aperture at this stage of prototype development reduces cost and complexity while all of the functionality can still be tested.

Figure 3a illustrates the proposed acoustic stack, which includes a matrix array made of lead zirconate titanate (PZT) piezoelectric material, the ASIC, a buffer layer, a matching layer, an aluminum ground foil, and a protective top layer. This stack design is similar to those we have described in our previous articles [24,32,44]. To determine the thickness of each layer within the stack, we conducted simulations using finite-element analysis software (PzFlex, Weidlinger Associates, Inc., Mountain View, CA, USA). To fabricate the acoustic stack, gold balls are first deposited onto the transducer bond pads of the ASIC. The gaps between the balls are filled with an electrically isolating epoxy material, which is then ground down until the gold balls are exposed again. A conductive glue matching layer is applied on top of the piezoelectric material (3203HD, CTS Corp., Lisle, IL, USA), followed by gluing of the PZT and matching layer stack onto the gold balls. The acoustical stack is then diced using a 20 μm dicing saw. To create a common ground electrode, 7-μm-thick aluminum foil is glued on top of the entire matrix array. Finally, to prevent moisture and damage, a thin layer of encapsulation material (AptFlex F7, Precision Acoustics Ltd., Dorchester, UK) is placed on top of the stack. Figure 3b is a photograph of the acoustic stack mounted on top of the ASIC and PCB before the ground foil is deposited.

Acoustic characterization

For the acoustic characterization and tests, the prototype was placed in a watertight box with a 25-μm-thick polyimide acoustic window and submerged in a water tank filled with deionized water. A custom motherboard was used to interface the prototype with a computer for data processing through commercial field programmable gate arrays (FPGAs), as illustrated in Figure 4.

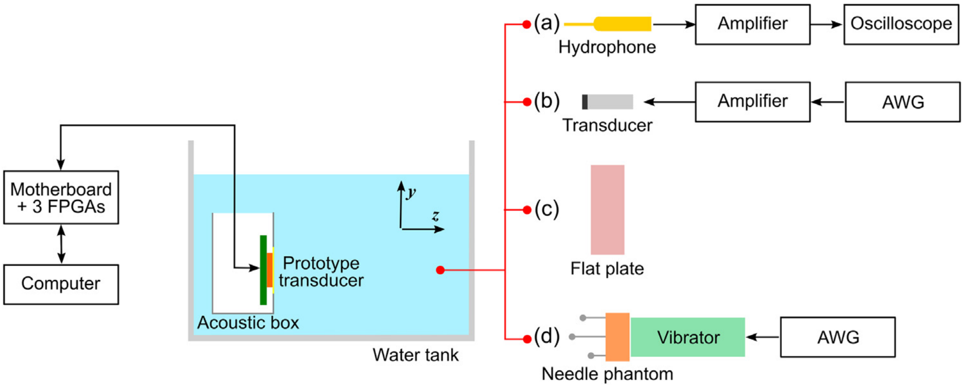

Figure 4. Measurement setup. (a) Transmit characterization. (b) Receive characterization. (c) Pulse−echo measurements. (d) Imaging.

To assess the transmit performance (Fig. 4a), we evaluated the time and frequency responses of individual transducer elements. For this, we applied 30 V pulses to the element under test and measured the resulting acoustic pressure generated by it using a calibrated 1 mm needle hydrophone (SN2082, Precision Acoustics Ltd.) placed at a distance of 5 cm from the transducer. The hydrophone output was then amplified by a 60 dB amplifier (AU-1519, Miteq, Inc., Hauppauge, NY, USA) and digitized by an oscilloscope (DSO-X 4024A, Agilent Technologies, Santa Clara, CA, USA). Next, we characterized the directivity pattern of specific transducer elements using hydrophone scans with a calibrated 0.2 mm needle hydrophone (SN3800, Precision Acoustics Ltd.). We performed rotational scans ranging from −60° to 60° at a distance of 5 cm from the transducer. Using the same setup, we evaluated the directivity pattern of the entire transducer when transmitting diverging waves steered at seven different angles in elevation. To provide a comprehensive assessment, we compared the measured directivity patterns with simulations performed using the ultrasound simulator FOCUS [45].

To assess the receive performance (Fig. 4b), we used a pre-calibrated 1 mm circular single-element transducer (PA865, Precision Acoustics Ltd.) as a transmitter placed 5 mm away from the prototype. We drove the single-element transducer with an 8-cycle sine wave generated by an arbitrary waveform generator (AWG; 33250A, Agilent Technologies) and measured the response at each individual element of the prototype to evaluate the sensitivity variation and element yield. With the same setup, we evaluated the dynamic range of the prototype, which is defined as the difference between the highest and lowest detectable pressures. Hence, we varied the surface pressure applied to the prototype between 1 Pa and 100 kPa while varying the gain setting of the ASIC from −6 to 48 dB. Lastly, we measured the directivity pattern of one subarray when pre-steering it at seven different angles in the elevation direction. For this, the prototype was rotated from −60° to 60° in increments of 1°. At each angle, the received data were transferred to the computer for processing.

For pulse−echo measurements (Fig. 4c), we positioned a quartz flat plate 5 cm from the prototype. A plane wave was transmitted with all elements excited with three cycles of 30 V, and the resulting echoes were received by each individual element.

High-frame-rate 3-D imaging

To assess the high-frame-rate 3-D imaging capability, we used a custom phantom consisting of three needles. The phantom was positioned at a distance of about 4 cm from the prototype transducer (Fig. 4d). To introduce motion into the system, we attached the phantom to a mechanical shaker (Type 4810, Brüel & Kjær, Nærum, Denmark) and applied a low-frequency sine vibration of 20 Hz. To capture the dynamic movement of the needles in 3-D, we acquired 280 pulse−echo cycles at a PRF of 7 kHz. As seven pulse−echo cycles are required to generate each 3-D volume image, a total of 40 volumetric images were obtained from the 280 pulse−echo cycles at a 1 kHz volumetric frame rate.

The received data were first digitized by the ADCs and subsequently transferred to the FPGA boards. After data acquisition, it was downloaded to the computer for processing, as detailed in Hopf et al. [43]. The reconstruction of the 3-D volume image was performed offline using conventional delay-and-sum operations with angular-weighted coherent compounding, as described in Soozande et al. [8].

To provide a comparison to the high-frame-rate 3-D imaging results, we used a commercial diagnostic ultrasound machine (Aplio Artida, Toshiba Medical Systems, Otawara, Japan) with a linear probe (PLT-704SBT, Toshiba Medical Systems) to measure the displacement of the needles using M-mode imaging.

Results

Transmit characterization

Figure 5a illustrates the time and frequency responses of five transducer elements recorded with the hydrophone. At 5 cm, the average peak pressure for a single element is about 0.85 kPa. In the frequency domain, the center frequency is about 5.5 MHz, and the average −6 dB bandwidth is about 60%. In Figure 5b, the directivity pattern of five elements together with the simulated curve along the elevation direction is illustrated. The experimental observations reveal a −6 dB beam width of approximately 55°, while the simulated result is about 112°. This deviation is due to the dips seen at approximately ±40° in the measured directivity. Similar results were observed along the azimuth direction as the element has a square geometry.

Figure 6 depicts the locally normalized directivity pattern of the entire matrix array transmitting diverging waves steered at seven different angles ranging from −30° to 30° in the elevation direction. The measured and simulated profiles are in good agreement, with a −6 dB beam width of approximately 20° observed in both cases. This confirms the effectiveness of the prototype in generating and steering diverging beams. In Figure 7, the directivity pattern along the azimuth direction is displayed for the current prototype and the full-size aperture. As seen, there is an excellent agreement between the measured and simulated profiles , with the −6 dB beam width of about 20° for the current aperture. For the full-size aperture, we observe a −6 dB beam width of about 70°, which is according to our design goal.

Receive characterization

Figure 8a illustrates the sensitivity variation in receive across all elements of the prototype transducer. The results indicate a high

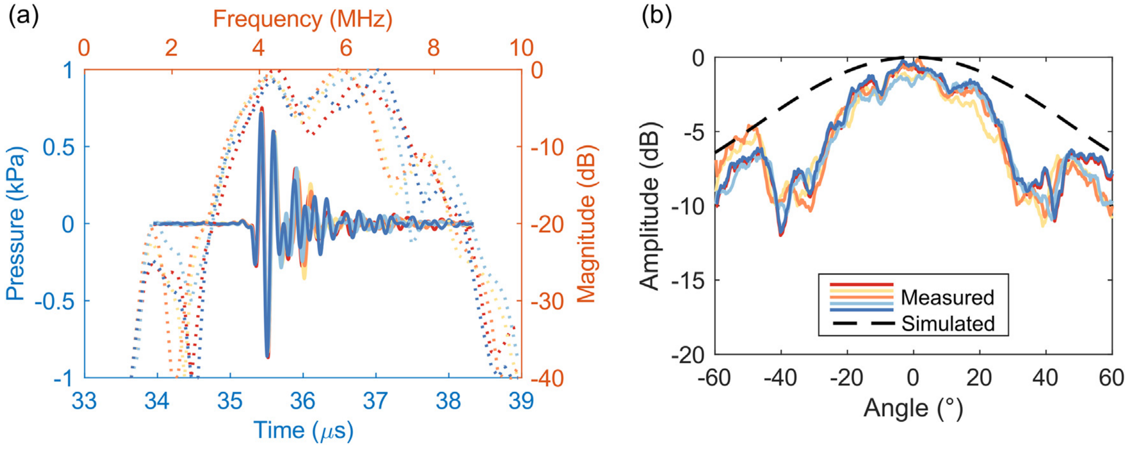

Figure 5. (a) Time and frequency responses of individual elements. (b) Measured and simulated directivity pattern of individual elements.

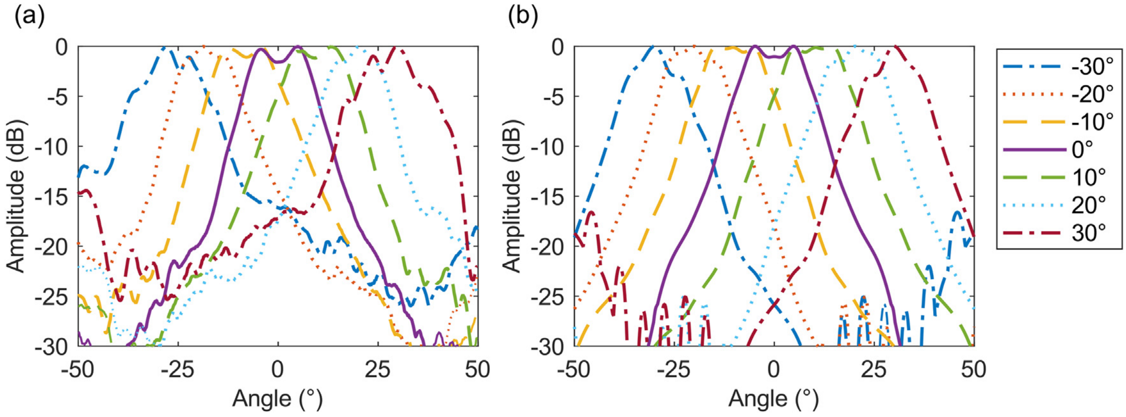

Figure 6. Directivity pattern of the transducer transmitting steered diverging waves in elevation. (a) Measured. (b) Simulated.

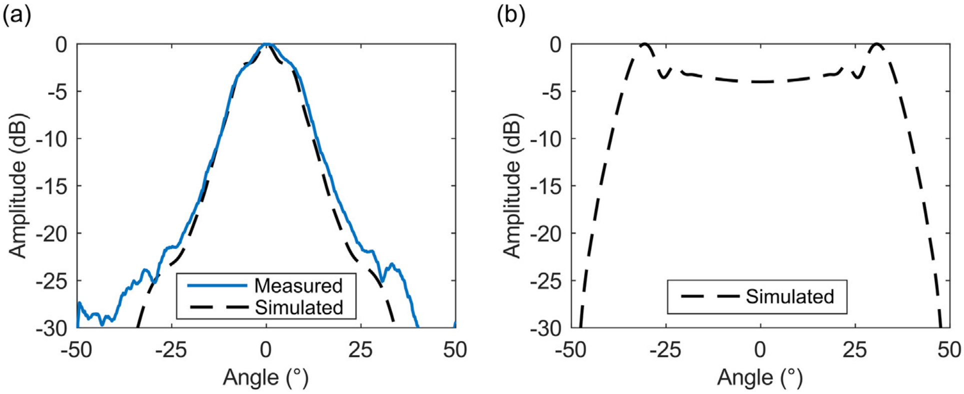

Figure 7. Directivity pattern of the transducer transmitting a diverging wave in azimuth. (a) Current aperture. (b) Full-size aperture.

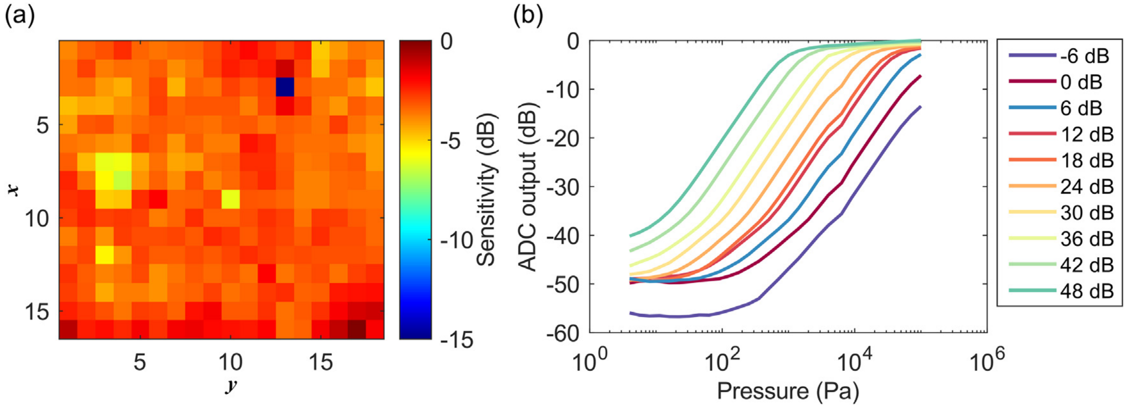

Figure 8. (a) Sensitivity variation in receive. (b) Relation between received pressure and ADC output for all ASIC gains.

yield, with 282 of 288 elements (*i.e.,* 98%) falling within the range of 0 to −6 dB. Only one element, indicated in *dark blue*, exhibits no signal and is considered defective in receive. Figure 8b illustrates the relationship between the received pressure at the surface of the prototype and the corresponding normalized ADC output for all gain levels. To reduce measurement time, the measurements were conducted using one-third of the array, that is, 96 elements. The plotted values represent the average across these 96 elements. The lowest detectable pressure is around 10 Pa, which was measured when the ASIC gain was set to 48 dB. The highest detectable pressure was about 100 kPa, which was measured for a gain of −6 dB. An overall dynamic range of about 80 dB is obtained between the 0 dB SNR point of the highest gain and the 1 dB compression point of the lowest gain setting.

Figure 9 illustrates the measured and simulated directivity patterns of a 1 × 3 subarray pre-steering at seven different angles, ranging from −30° to 30° in the elevation direction. The measured and simulated profiles exhibit good agreement, which indicates that the designed ASIC can efficiently generate the necessary delays to steer the subarrays toward the intended directions. The measured −6 dB beam width is approximately 40° for all steering angles, except for −30° steering, which has a beam width of about 50°. In simulations, the −6 dB beam width is 56° when there is no steering and about 35° for the other steering angles. Note that as the steering angle increases, the side lobe levels tend to rise too.

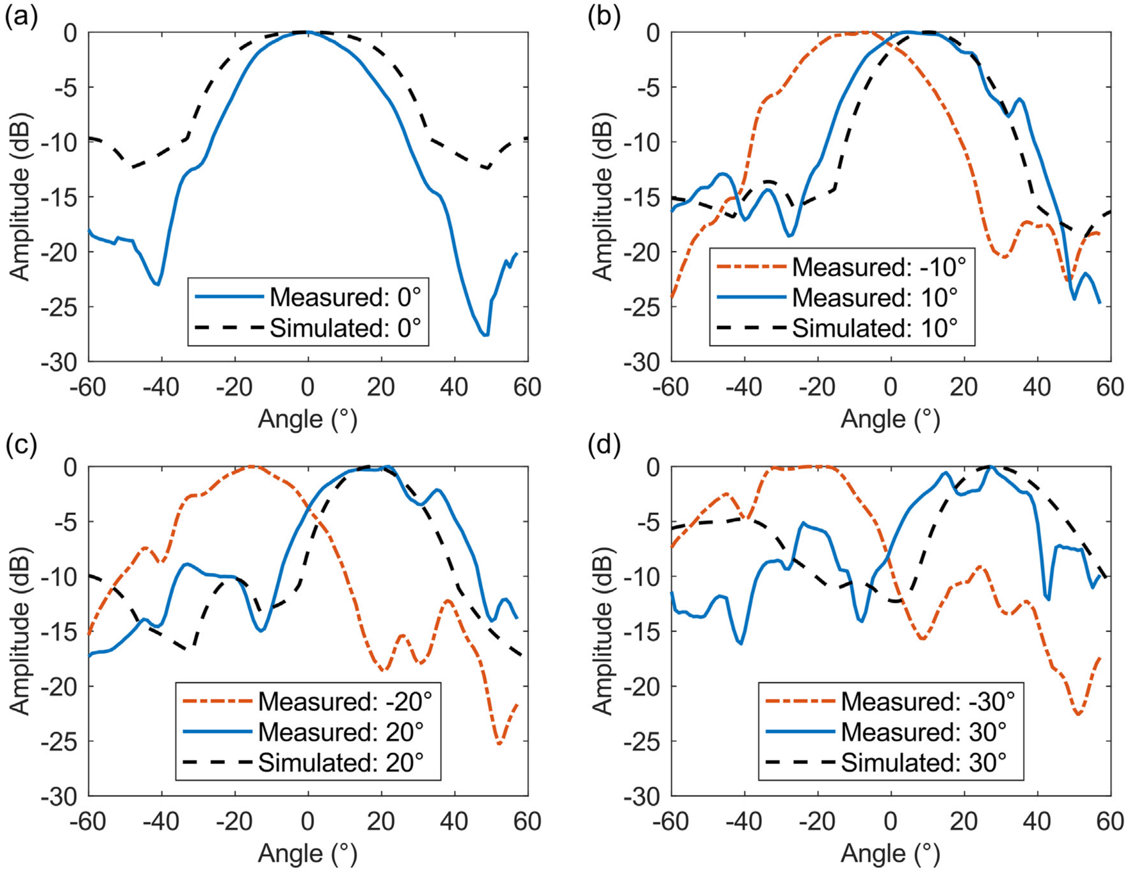

Figure 9. Measured and simulated directivity pattern of a 1 × 3 subarray pre-steered at (a) 0°, (b) ±10 °, (c) ±20° and (d) ±30° in the elevation direction.

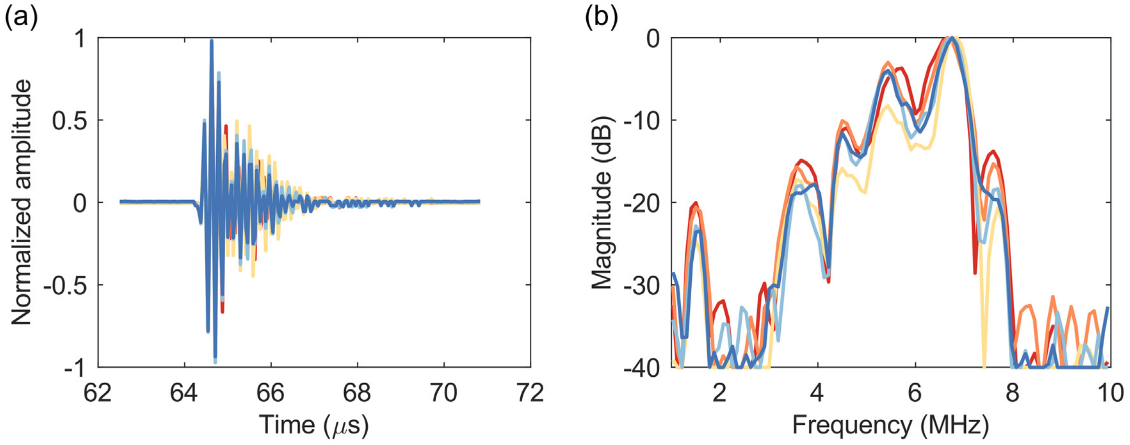

Figure 10. Pulse−echo responses obtained from 3-cycle transmissions using all elements and a single-element receiver. (a) Time domain. (b) Frequency domain.

Pulse−echo measurements

Figure 10 illustrates the pulse−echo measurements obtained by transmitting three cycles with all elements (no steering) and receiving the echo with individual elements without applying micro-beamforming. The measurements were conducted using five arbitrarily selected elements as receivers. All measured elements exhibit a comparable amplitude response and a center frequency of about 6.1 MHz. Note that a dip around 6 MHz causes the −6 dB bandwidth to narrow to roughly 10%.

Imaging

Figure 11 shows one of the 40 volumetric images of the needle phantom captured by our prototype transducer at a frame rate of 1000 volumes/s. After the acquisition, the data were transferred from the motherboard to a computer for offline image processing. The reconstructed image clearly distinguishes the needles in 3-D space, and the positions of the point scatterers closely match the position of the needles in the photograph of the phantom. Note, however, that each imaged needle exhibits one main lobe accompanied by secondary lobes in both the azimuth and elevation directions.

We used the data set consisting of 40 images to track the axial motion of a single needle to show the high-frame-rate imaging capability of the ASIC. Figure 12a illustrates the resulting displacement of one needle, and Figure 12b, its instantaneous velocity derived by pulsed-wave Doppler processing of the high-frame-rate images. The 20 Hz vibration of the needle is clearly visible, and we were able to capture about 80% of its sinusoidal motion within the 40 ms

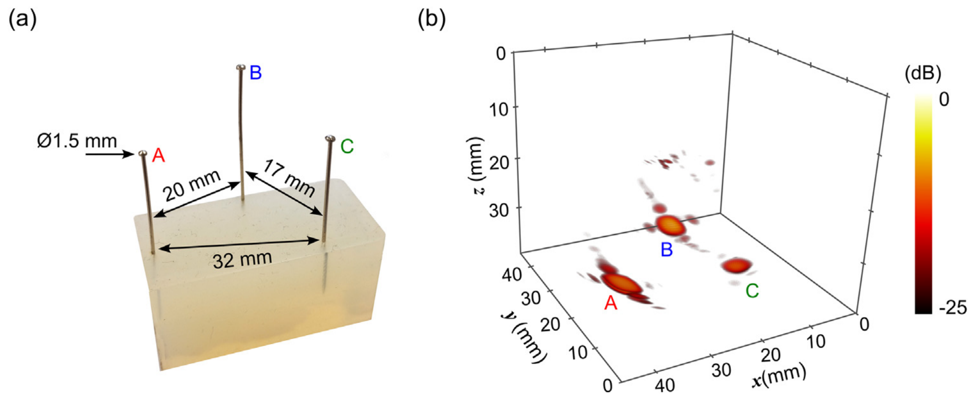

Figure 11. (a) Photograph of the needle phantom. (b) Reconstructed 3-D image acquired with the prototype at a frame rate of 1000 volumes/s.

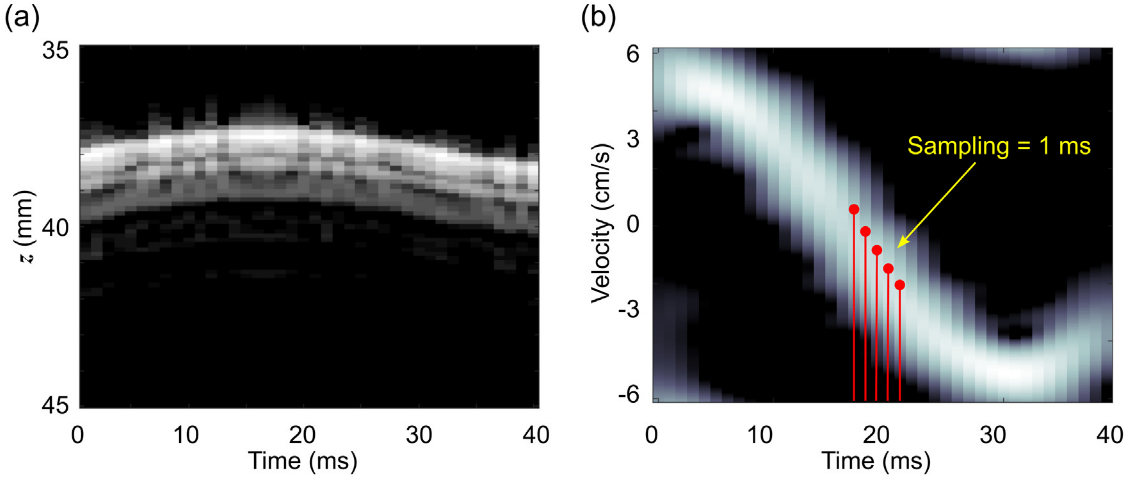

Figure 12. Motion of a single needle extracted from high-frame-rate 3-D images acquired with the prototype transducer. (a) Needle displacement. (b) Needle velocity.

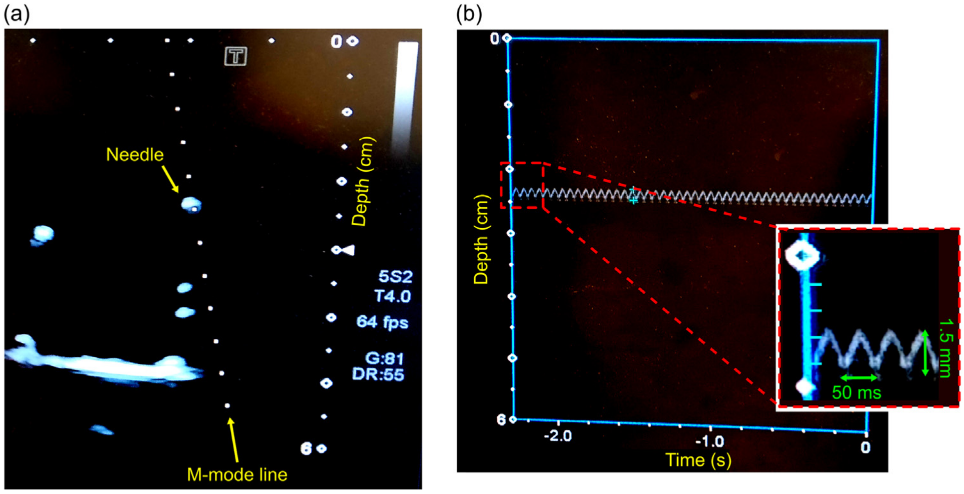

Figure 13. Images of the needle phantom acquired with the Toshiba system. (a) B-mode image. (b) M-mode image.

acquisition time. We observed a peak-to-peak displacement of approximately 1.5 mm, with a maximum measured velocity of around 5 cm/s.

In Figure 13a is the B-mode image of the needle phantom acquired with the commercial imaging system, which was used for validation. To track the motion of one of the needles, we drew a line on it and performed M-mode imaging, as depicted in Figure 13b. The 20 Hz vibration of the needle is also evident, and we measured the same peak-to-peak displacement of about 1.5 mm. This agreement highlights our capability to achieve high-frame-rate 3-D imaging.

Discussion

We have described the development of a high-frame-rate 3-D imaging prototype ICE transducer. This involved constructing a PZT matrix array with 16 × 18 elements interfaced with a pitch-matched ASIC. To address the challenge of cable count reduction, we implemented subarray beamforming in receive and on-chip digitization, and used a combination of TDM and PAM data transmission. This allowed us to reduce the total cable count by 18-fold lower than the acoustic element number, resulting in a feasible number of cables for practical implementation. Because of complexity and cost constraints, we built a prototype that corresponds to a quarter of the full-size aperture design (64 × 18), and the transducer was mounted on a PCB for convenience. Despite these modifications, we were able to conduct comprehensive tests to examine the prototype's performance and verify its functionality.

As depicted in Figure 5a, the responses of the five individual elements exhibit similar behavior in transmit. At a distance of 5 cm, each element has a transmit efficiency of around 28 Pa/V, which is consistent with previous designs [32,44]. On average, the center frequency of the elements is 5.5 MHz, and the −6 dB bandwidth is 60% in transmit. Note that the frequency spectrum exhibits a dip at approximately the center frequency, which decreases the overall bandwidth. This dip is also observed in the pulse−echo response, illustrated in Figure 10, and is likely the result of reflections and standing waves from the ASIC, as we have previously investigated through simulations [44,46]. To mitigate this effect, an interposer layer between the PZT and the ASIC could be used [6,44,47]. We may explore this option in future designs.

The directivity pattern of the single elements, as illustrated in Figure 5b, generally follows the trend of the simulated directivity. However, we observed dips at ±40°, which is likely caused by acoustic crosstalk [48,49], as we have previously reported [44,46]. Note that the measured electric crosstalk for this probe is about −75 dB between channels, as determined in our previous work [26]. The directivity pattern of the entire transducer, as illustrated in Figures 6 and 7, aligns very well with simulations and demonstrates that the prototype is capable of steering from −30° to 30° in the elevation direction. Considering that the azimuth aperture is extended as originally designed (*i.e.,* with 64 elements), our prototype is expected to provide a coverage of 70° × 70°. In receive, the directivity pattern of the 1 × 3 subarrays (Fig. 9) also exhibits the expected behavior, albeit with an increase in degradation and artifacts at higher steering angles [50]. Overall, the directivity pattern measurements confirm that the ASIC is effective in generating the desired delay patterns, as specified in our design.

The sensitivity map depicted in Figure 8a reveals that 282 of 288 elements of the prototype are within the −6 dB range. This element yield of 98% indicates the efficacy of our fabrication process and encourages us to consider scaling up the aperture size to 64 × 18 elements in future developments. In Figure 8b, we observed that the lowest detectable pressure of 10 Pa is limited by the ASIC's noise floor for a gain setting of 48 dB, whereas the highest detectable pressure of 100 kPa is limited by the ASIC's saturation level for a gain of −6 dB. This results in a total dynamic range of 80 dB, which is suitable for ICE. The measured peak SNR for the receive path is 52.2 dB [43]. Note that there seems to be an overlap in the gain step between 12 and 18 dB, which is not consistent with the expected 6 dB difference. This is likely due to a mismatch in the amplifier circuitry which can be easily corrected for in a future re-adjustment of design.

In the imaging experiment with the vibrating needle phantom, we successfully acquired 40 volumes within a 40 ms interval, achieving the intended frame rate of 1000 volumes/s. The reconstructed 3-D image of the needles depicted in Figure 11 confirms the prototype's 3-D imaging capabilities, even though some side lobes are present in the image. Nonetheless, it is worth noting that for the full-size array, the side lobes will be reduced and the overall imaging quality will be improved. By analyzing the 40 acquired volumetric images, we were able to extract the motion pattern of the needle and accurately estimate its velocity with retrospective pulsed-wave Doppler analysis, as illustrated in Figure 12. The clean Doppler spectrogram indicates proper internal timing and digitization of the signals. These results are very promising, as we were able to precisely validate them with a clinical ultrasound system as a reference (Fig. 13).

As the ICE prototype transducer is currently mounted on a large PCB for testing purposes, it is not yet ready for (pre)clinical use. In future work, we plan to assemble a complete prototype and integrate it into a catheter for EWI validation.

Conclusions

In this study, we have presented the design, fabrication and characterization of a prototype transducer with an integrated ASIC for high-frame-rate 3-D ICE. By applying subarray beamforming alongside on-chip digitization time-division multiplexing and pulse amplitude modulation data transmission, we were able to significantly reduce the cable count to a realistic number that can fit within a catheter shaft. The acoustic performance of the prototype met the design requirements, allowing us to achieve 3-D imaging with a large field of view and a frame rate of 1000 volumes/s. This high frame rate outperforms current state-of-the-art ICE probes and paves the way toward implementation of electromechanical wave imaging on future ICE catheters. Future work should focus on realizing a full aperture transducer inside a catheter to enable *in vivo* testing.

Conflict of interest

The authors declare no competing interests.

Acknowledgments

This research is part of the 3D-ICE and UltraXtreme projects (Project Nos. 14279 and P17-32, respectively), which are partly financed by the Netherlands Organization for Scientific Research (NWO).

Data availability statement

The data presented in this study are available on request from the corresponding author.

References

[1] Jalife J. Mother rotors and fibrillatory conduction: a mechanism of atrial fibrillation. Cardiovasc Res 2002;54:204–16.
[2] Go AS, Hylek EM, Phillips KA, Chang Y, Henault LE, Selby JV, et al. Prevalence of diagnosed atrial fibrillation in adults. JAMA 2001;285:2370.
[3] Krijthe BP, Kunst A, Benjamin EJ, Lip GYH, Franco OH, Hofman A, et al. Projections on the number of individuals with atrial fibrillation in the European Union, from 2000 to 2060. Eur Heart J 2013;34:2746–51.
[4] Kheiri B, Simpson TF, Przybylowicz R, Merrill M, Alhamoud H, Osman M, et al. Ablation versus antiarrhythmic drugs as first-line treatment of paroxysmal atrial fibrillation: a meta-analysis of randomized trials. Circ Arrhythm Electrophysiol 2021;14:305–15.
[5] Katritsis G, Calkins H. Catheter ablation of atrial fibrillation—techniques and technology. Arrhythm Electrophysiol Rev 2012;1:29.
[6] Wildes D, Lee W, Haider B, Cogan S, Sundaresan K, Mills DM, et al. 4-D ICE: a 2-D array transducer with integrated ASIC in a 10-Fr catheter for real-time 3-D intracardiac echocardiography. IEEE Trans Ultrason Ferroelectr Freq Control 2016;63:2159–73.
[7] Cooper JM, Epstein LM. Use of intracardiac echocardiography to guide ablation of atrial fibrillation. Circulation 2001;104:3010–3.
[8] Soozande M, Ossenkoppele BW, Hopf Y, Pertijs MAP, Verweij MD, de Jong N, et al. Imaging scheme for 3-D high-frame-rate intracardiac echography: a simulation study. IEEE Trans Ultrason Ferroelectr Freq Control 2022;69:2862–74.
[9] Lee W, Idriss SF, Wolf PD, Smith SW. A miniaturized catheter 2-D array for real-time, 3-D intracardiac echocardiography. IEEE Trans Ultrason Ferroelectr Freq Control 2004;51:1334–46.
[10] Pua EC, Idriss SF, Wolf PD, Smith SW. Real-time 3D transesophageal echocardiography. Proc IEEE Ultrason Symp 2004:778–81.
[11] La Greca C, Cirasa A, Di Modica D, Sorgato A, Simoncelli U, Pecora D. Advantages of the integration of ICE and 3D electroanatomical mapping and ultrasound-guided femoral venipuncture in catheter ablation of atrial fibrillation. J Interv Card Electrophysiol 2021;61:559–66.
[12] Provost J, Lee WN, Fujikura K, Konofagou EE. Imaging the electromechanical activity of the heart in vivo. Proc Natl Acad Sci USA 2011;108:8565–70.
[13] Konofagou EE, Provost J. Electromechanical wave imaging for noninvasive mapping of the 3D electrical activation sequence in canines and humans in vivo. J Biomech 2012;45:856–64.

[14] Provost J, Nguyen VTH, Legrand D, Okrasinski S, Costet A, Gambhir A, et al. Electromechanical wave imaging for arrhythmias. Phys Med Biol 2011;56:L1–11.

[15] Provost J, Gurev V, Trayanova N, Konofagou EE. Mapping of cardiac electrical activation with electromechanical wave imaging: an in silico−in vivo reciprocity study. Heart Rhythm 2011;8:752–9.

[16] Provost J, Costet A, Wan E, Gambhir A, Whang W, Garan H, et al. Assessing the atrial electromechanical coupling during atrial focal tachycardia, flutter, and fibrillation using electromechanical wave imaging in humans. Comput Biol Med 2015;65:161–7.

[17] Costet A, Wan E, Bunting E, Grondin J, Garan H, Konofagou E. Electromechanical wave imaging (EWI) validation in all four cardiac chambers with 3D electroanatomic mapping in canines in vivo. Phys Med Biol 2016;61:8105–19.

[18] Allessie M, de Groot N. CrossTalk opposing view: rotors have not been demonstrated to be the drivers of atrial fibrillation. J Physiol 2014;592:3167–70.

[19] Pope MTB, Kuklik P, Briosa e Gala A, Leo M, Mahmoudi M, Paisey J, et al. Spatial and temporal variability of rotational, focal, and irregular activity: practical implications for mapping of atrial fibrillation. J Cardiovasc Electrophysiol 2021;32:2393–403.

[20] Bessiere F, Zorgani A, Daunizeau L, Cao E, Vaillant F, Abell E, et al. High frame rate ultrasounds for electromechanical wave imaging to characterize and differentiate endocardial from epicardial activation of ventricular arrhythmia: a proof of concept study. Arch Cardiovasc Dis 2019;11:259. Suppl.

[21] Savord B, Solomon R. Fully sampled matrix transducer for real time 3D ultrasonic imaging. Proc IEEE Ultrason Symp 2003;1:945–53.

[22] Chen C, Chen Z, Bera D, Noothout E, Chang ZY, Tan M, et al. A pitch-matched front-end ASIC with integrated subarray beamforming ADC for miniature 3-D ultrasound probes. IEEE J Solid-State Circuits 2018;53:3050–64.

[23] Carpenter TM, Rashid MW, Ghovanloo M, Cowell DMJ, Freear S, Degertekin FL. Direct digital demultiplexing of analog TDM signals for cable reduction in ultrasound imaging catheters. IEEE Trans Ultrason Ferroelectr Freq Control 2016;63:1078–85.

[24] Kang E, Ding Q, Shabanimotlagh M, Kruizinga P, Chang ZY, Noothout E, et al. A reconfigurable ultrasound transceiver ASIC with 24 × 40 elements for 3-D carotid artery imaging. IEEE J Solid-State Circuits 2018;53:2065–75.

[25] Chen C, Chen Z, Bera D, Raghunathan SB, Shabanimotlagh M, Noothout E, et al. A front-end ASIC with receive sub-array beamforming integrated with a 32 × 32 PZT matrix transducer for 3-D transesophageal echocardiography. IEEE J Solid-State Circuits 2017;52:994–1006.

[26] Hopf YM, Ossenkoppele BW, Soozande M, Noothout E, Chang ZY, Chen C, et al. A pitch-matched transceiver ASIC with shared hybrid beamforming ADC for high-frame-rate 3-D intracardiac echocardiography. IEEE J Solid-State Circuits 2022;57:3228–42.

[27] Lee J, Lee KR, Eovino BE, Park JH, Liang LY, Lin L, et al. A 36-channel auto-calibrated front-end ASIC for a pMUT-based miniaturized 3-D ultrasound system. IEEE J Solid-State Circuits 2021;56:1910–23.

[28] Li J, Chen Z, Tan M, van Willigen D, Chen C, Chang ZY, et al. A 1.54mW/element 150μm-pitch-matched receiver ASIC with element-level SAR/shared-single-slope hybrid ADCs for miniature 3D ultrasound probes. 2019 Symposium on VLSI Circuits. New York: IEEE; 2019. p. C220–1.

[29] Kaplan RM, Narang A, Gay H, Gao X, Gibreal M, Arora R, et al. Use of a novel 4D intracardiac echocardiography catheter to guide interventional electrophysiology procedures. J Cardiovasc Electrophysiol 2021;32:3117–24.

[30] Kim YH, Collins J, Li Z, Chinnadurai P, Kapoor A, Lin CH, et al. Automated catheter tip repositioning for intra-cardiac echocardiography. Int J Comput Assist Radiol Surg 2022;17:1409–17.

[31] Della Rocca DG, Gianni C, Magnocavallo M, Mohanty S, Bassiouny MA, Gallinghouse GJ, et al. PO-696-06 real-world experience with a novel 3D intracardiac echocardiography catheter. Heart Rhythm 2022;19:S419–20.

[32] Daeichin V, Bera D, Raghunathan S, Shabani Motlagh M, Chen Z, Chen C, et al. Acoustic characterization of a miniature matrix transducer for pediatric 3D transesophageal echocardiography. Ultrasound Med Biol 2018;44:2143–54.

[33] de Jong N, Bom N, Souquet J, Faber G. Vibration modes, matching layers and grating lobes. Ultrasonics 1985;23:176–82.

[34] Ellens N, Pulkkinen A, Song J, Hynynen K. The utility of sparse 2D fully electronically steerable focused ultrasound phased arrays for thermal surgery: a simulation study. Phys Med Biol 2011;56:4913–32.

[35] Ramalli A, Boni E, Savoia AS, Tortoli P. Density-tapered spiral arrays for ultrasound 3-D imaging. IEEE Trans Ultrason Ferroelectr Freq Control 2015;62:1580–8.

[36] Chen K, Lee HS, Sodini CG. A column-row-parallel ASIC architecture for 3-D portable medical ultrasonic imaging. IEEE J Solid-State Circuits 2016;51:738–51.

[37] Flesch M, Pernot M, Provost J, Ferin G, Nguyen-Dinh A, Tanter M, et al. 4D in vivo ultrafast ultrasound imaging using a row-column addressed matrix and coherently-compounded orthogonal plane waves. Phys Med Biol 2017;62:4571–88.

[38] Wei L, Wahyulaksana G, Meijlink B, Ramalli A, Noothout E, Verweij MD, et al. High frame rate volumetric imaging of microbubbles using a sparse array and spatial coherence beamforming. IEEE Trans Ultrason Ferroelectr Freq Control 2021;68:3069–81.

[39] Bouzari H, Engholm M, Beers C, Stuart MB, Nikolov SI, Thomsen EV, et al. Curvilinear 3-D imaging using row-column-addressed 2-D arrays with a diverging lens: phantom study. IEEE Trans Ultrason Ferroelectr Freq Control 2018;65:1182–92.

[40] Papadacci C, Pernot M, Couade M, Fink M, Tanter M. High-contrast ultrafast imaging of the heart. IEEE Trans Ultrason Ferroelectr Freq Control 2014;61:288–301.

[41] Hopf YM, Ossenkoppele B, Soozande M, Noothout E, Chang ZY, Vos HJ, et al. A compact integrated high-voltage pulser insensitive to supply transients for 3-D miniature ultrasound probes. IEEE Solid State Circuits Lett 2022;5:166–9.

[42] Hopf YM. Integrated circuits for 3D high-frame-rate intracardiac echocardiography probes. Delft University of Technology; 2023 PhD thesis.

[43] Hopf YM, dos Santos DS, Ossenkoppele BW, Soozande M, Noothout E, Chang ZY, et al. A pitch-matched high-frame-rate ultrasound imaging ASIC for catheter-based 3-D probes. IEEE J Solid-State Circuits 2023:1–16.

[44] dos Santos DS, Fool F, Mozaffarzadeh M, Shabanimotlagh M, Noothout E, Kim T, et al. A tiled ultrasound matrix transducer for volumetric imaging of the carotid artery. Sensors 2022;22:9799.

[45] McGough RJ. Rapid calculations of time-harmonic nearfield pressures produced by rectangular pistons. J Acoust Soc Am 2004;115:1934–41.

[46] Shabanimotlagh M, Daeichin V, Raghunathan SB, Kruizinga P, Vos HJ, Bosch JG, et al. Optimizing the directivity of piezoelectric matrix transducer elements mounted on an ASIC. Proc IEEE Int Ultrason Symp 2017:5–8.

[47] Wodnicki R, Kang H, Chen R, Cabrera-Munoz NE, Jung H, Jiang L, et al. Co-integrated PIN-PMN-PT 2-D array and transceiver electronics by direct assembly using a 3-D printed interposer grid frame. IEEE Trans Ultrason Ferroelectr Freq Control 2020;67:387–401.

[48] Celmer M, Opieliński KJ. Research and modeling of mechanical crosstalk in linear arrays of ultrasonic transducers. Arch Acoust 2016;41:599–612.

[49] Bybi A, Khouili D, Granger C, Garoum M, Mzerd A, Hladky-Hennion AC. Experimental characterization of a piezoelectric transducer array taking into account crosstalk phenomenon. International Journal of Engineering and Technology Innovation 2020;10:1–14.

[50] Wooh SC, Shi Y. Optimum beam steering of linear phased arrays. Wave Motion 1999;29:245–65.